FEM-assisted shearography with spatially modulated heating for non-destructive testing of thick composites with deep defects

Tao, Nan; Anisimov, Andrei G.; Groves, Roger M.

DOI
10.1016/j.compstruct.2022.115980

Publication date
2022

Document Version
Final published version

Published in
Composite Structures

Composite Structures 297 (2022) 115980

Contents lists available at ScienceDirect

Composite Structures

journal homepage: www.elsevier.com/locate/compstruct

FEM-assisted shearography with spatially modulated heating for non-destructive testing of thick composites with deep defects

Nan Tao *, Andrei G. Anisimov, Roger M. Groves

Aerospace NDT Laboratory, Faculty of Aerospace Engineering, Delft University of Technology, Kluyverweg 1, 2629 HS Delft, the Netherlands

ARTICLE INFO

Keywords:
Thick composite
NDT
FEM
Global heating (GH)
Spatially modulated heating (SMH)

ABSTRACT

This study aims at improving shearography non-destructive testing (NDT) of deep defects in thick composites with thermal loading. Instead of conventional global heating (GH), the core idea is to apply novel spatially modulated heating (SMH) for shearography NDT. In this paper, the finite element method (FEM) has been used to advance shearography towards a quantitative inspection tool for thick composites. Both GH and SMH have been performed experimentally and modelled in Abaqus to evaluate the corresponding efficacies in the detection of deep defects. SMH was achieved by using a halogen lamp with a Fresnel lens. The heat flux distribution on the specimen surface was taken into consideration for defect detection, a factor which is rarely reported in shearography inspection. Besides, the influence of different reference states on shearography NDT of deep defects in thick composites has also been studied by looking into the defect-induced phase maps from shearography. The results indicate that the proposed SMH can improve deep defect detection with shearography in thick composites by 2 to 3 times that of GH. It should be addressed that a similar and defect-free reference sample is currently necessary to compare with a defective one.

1. Introduction

Thick composite structures [1–4] have found increasing applications in a diverse range of areas due to their excellent advantages of weight savings, high strength, high stiffness, and resistance to corrosion and fatigue. In the aerospace industry, carbon fiber reinforced composites (CFRP) have been applied to wings and fuselages [1,2,5] as well as primary loading-bearing structures [2]. For instance in the Airbus A380, the thickness of the composite components at the wing root joint could be up to 45 mm [6]. In the marine sectors, glass fiber reinforced composites (GFRP) are seeing widespread applications in large-scale structures including ship superstructures, decks, and hulls [3,4]. As an example, sandwich composites made from glass-fiber laminate skins with polyvinyl chloride (PVC)-foam core are common in use for the construction of large hull structures whose thickness can easily go to more than 100 mm. In wind energy, glass fiber and carbon fiber reinforced composites are used in blades and foundations of offshore wind turbines [2,7]. A prototype offshore wind turbine blade (100 m long) made from fiber-reinforced composites can have a cross-section up to 76 mm thick [8].

Although successful applications of thick composites are extensive, nevertheless, various defects including delaminations and fiber breakage may occur both during the manufacturing process and in service due to material complexity. For example, residual stresses that arise from resin shrinkage and uneven cure in manufacturing can lead to delaminations, fiber–matrix debonding, fiber waviness, and matrix cracking in thick composites [9]. Accidental impacts in service can also cause internal delaminations and matrix cracking which are barely visible from the impact surface [2,10]. Those defects, which can be at the surface or near-surface, as well as deeply buried, may have significant effects on the mechanical performance and the structural integrity of thick composites [1,11]. Hence, non-destructive testing (NDT) of thick composites is of significant importance for improving structural safety and reliability. Some well-known NDT techniques, such as ultrasonic testing [5,12] and X-ray [13–15], have trouble performing an on-site inspection, e.g. in the shipyard environment [11], and it can take a long time to scan an entire structure (e.g. ship hull) [11]. Other common NDT techniques, e.g. vibration analysis [16,17] and thermography [11,18,19], have their limitations as well. Vibration analysis, including low-frequency resonance and mechanical impedance techniques, suffers from detecting defects in structures with high stiffness, which means thick laminates or defects at significant depth are difficult or impossible

* Corresponding author.
E-mail address: n.tao@tudelft.nl (N. Tao).

https://doi.org/10.1016/j.compstruct.2022.115980
Received 8 March 2022; Received in revised form 13 June 2022; Accepted 6 July 2022
Available online 16 July 2022

to detect [1,2]. In thermography with thermal excitation, the ability to detect deeply buried defects in thick composites is limited due to the problems of rapid heat dissipation and non-uniform heating [1,2]. The characterization limit of inspection depth with thermography in polymer-matrix composite laminates appears to be less than 5 mm [1,2]. Overall, it is concluded that thick composite inspection remains an appealing problem and is an important and challenging task to implement [1,2].

Among the different kinds of NDT techniques, shearography [20–22] is an optical metrology method that is used to characterize surface strain components under loading. It offers the advantages of full-field measurement, non-contact inspection, and high sensitivity to deformation change. This technique has been used for qualitative inspection of delaminations, debonding, and other defects in thin composite materials [23–26]. It reveals defects in an object by looking for defect-induced deformation anomalies in the surface strain field. The surface strain field is obtained by comparing two deformation states of the test object. The reference status can be measured before loading, during loading, or after loading, and the signal status is usually measured after loading. Excitation methods used during shearography testing include thermal, vacuum, pressure, vibrational, microwave and impact excitations [21,27]. In this study, we focus on thermal loading [25,28–30] because of its advantages of being non-contact, its versatility, cost-effectiveness, and convenience for on-site inspection. Conventionally, global heating is applied to deform the object [25,28]. The distribution of heat flux over the surface of the test object is rarely considered in the shearography inspection. In literature, the finite element method (FEM) has been used to assist in the shearography NDT, which has enabled the prediction of thermal deformation during the inspection. In some cases, thermal loading was simulated by applying a temperature in the model to study shearography NDT of isotropic materials [25,28]. More recently, constant heat flux was used as an input of thermal loading for shearography inspection of an anisotropic wooden panel [31] as well as a CFRP plate [32], where heating was assumed to be uniform or locally uniform. However, in reality, the heat flux on the specimen surface can vary with location, which may affect defect detection. Moreover, for shearography NDT of thick composites, especially when detecting deeply buried defects (e.g. defect depth of 25 mm and more), the performance of conventional global heating may be less desirable. This is because the limitation of the thermal excitation method in thermography (i.e. rapid heat dissipation and non-uniform heating) also exists in shearography with conventional heating, which can affect inspection results. Therefore, a modulated heating process can be necessary in order to improve deep defect detection in thick composites.

It can be noted that the aforementioned studies with shearography were limited to thin isotropic or composite plates; few studies are available on shearography NDT of thick composites with thermal loading [33–35]. Our recent study has broadened the application of shearography with thermal loading to composites with thicknesses up to 50–60 mm [34], where the artificial defects are from 5 to 20 mm in depth which are represented by flat-bottom holes which can be detected in a 51 mm thick marine GFRP laminate. Nevertheless, deep defect detection was not studied in detail and the heat flux was assumed to be uniform in this modelling.

This work aims at improving the detection of deeply buried defects in thick composite laminates. For that, FEM-assisted shearography with spatially modulated heating (SMH) and conventional global heating (GH) have been conducted and investigated. A flat-bottom hole is used, following a standard practice [23–25], to indicate the major defect in a 51 mm thick GFRP laminate. Section 2 introduces the test GFRP panel, shearography theory and the experimental system. Section 3 presents the FEM model for predicting the thermal–mechanical response of the thick GFRP laminate during the inspection. Results and discussions are presented in Section 4. First in Section 4.1, we validate the model by comparing experimental and numerical results of the test GFRP panel subjected to GH and SMH, respectively. Afterward, we present defect-induced responses subjected to these thermal excitations in Section 4.2. The selection of the reference status on shearography NDT of the deep defect in the thick composite is discussed in Section 4.3. Conclusions are given in Section 5.

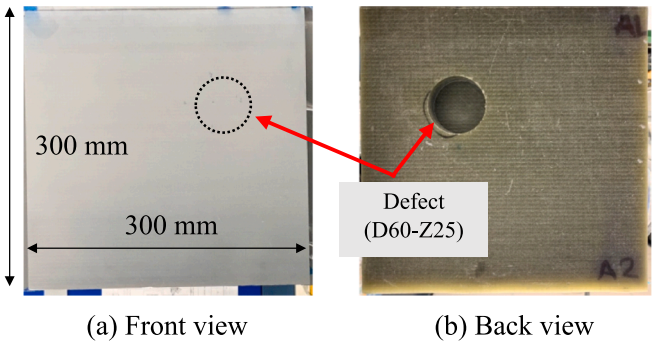

Fig. 1. The test GFRP specimen for shearography NDT (defect marked in a black dotted circle in (a)).

2. Specimen description and shearography

2.1. Specimen description

A 300 × 300 × 51 mm^3 GFRP laminate of E-glass/vinylester with the layup of $[0/+45/90/-45]_{60}$ is shown in Fig. 1. It is a representative test specimen for composite ship construction. The front and the back views of the thick GFRP laminate are shown in Fig. 1(a) and 1(b), respectively. The front surface of the specimen [Fig. 1(a)] was sprayed with removable white paint to increase the scattered light for the shearography inspection. To reliably simulate the major defect in the thick composite, a flat-bottom hole was made from the back surface of the specimen [Fig. 1(b)] to represent single delamination. The diameter and the remaining thickness of the hole are 60 and 25 mm, respectively, indicating that the artificial defect is 60 mm in size (D) and at 25 mm depth (Z). It should be noted that the defect size and depth are representative for deeply buried defects in marine composites. The material properties in different directions (e.g. Young's modulus, shear modulus, Poison's ratios, and thermal conductivities) can be found in [34].

2.2. Shearography theory and the instrument

During the shearography inspection, a laser beam was expanded to illuminate the surface of the specimen, creating a speckle pattern. By using a shearing device [Fig. 2(c)], the scattered laser light from two neighboring points on the specimen surface interfere at the camera to produce the interferogram. The shearing device enables temporal phase-shifting for obtaining the optical phase (ϕ) of the recorded speckle interferograms.

As mentioned in the introduction, shearography measures the displacement derivatives by comparing two deformation states of the specimen:

$$\delta\phi(x,y) = \phi'(x,y) - \phi(x,y) \tag{1}$$

where ϕ' and ϕ represent optical phases at pixel (x, y) of the two deformation states, and $\delta\phi$ represents their phase difference. For a shearography system with the main sensitivity to the out-of-plane deformation [Fig. 2(a)], the phase difference ($\delta\phi$) can be related just to the out-of-plane strain components (i.e., $\partial w/\partial x$ and $\partial w/\partial y$) [20,36]. Taking the shearing direction parallel to the x-axis as an example, the phase difference can be written as:

$$\delta\phi_x(x,y) = \frac{4\pi}{\lambda}\frac{\partial w(x,y)}{\partial x}\delta x(x,y) \tag{2}$$

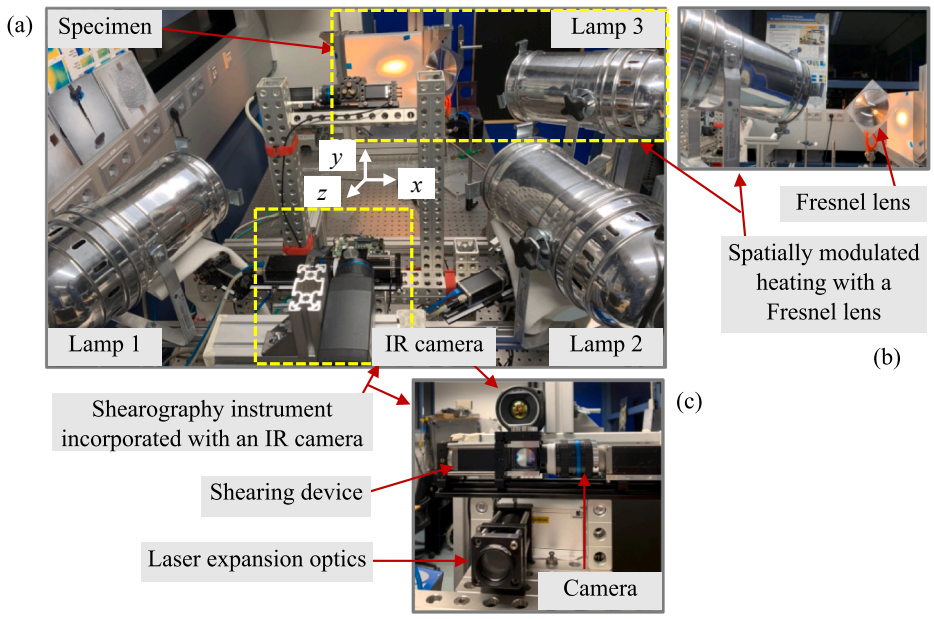

Fig. 2. Experimental shearography system for thick composite inspection: (a) an overview of the shearography instrument with conventional global heating (lamps 1, 2) and spatially modulated heating (lamp 3), (b) spatially modulated heating with a Fresnel lens, (c) shearography instrument incorporated with the IR camera.

where λ is the wavelength of the laser and δx is the amount of shearing in the x-direction.

Based on Eqs. (1) and (2), the phase difference ($\delta\phi$) can be retrieved pixel-by-pixel, producing a phase map corresponding to the reference status, and then, the strain component ($\partial w/\partial x$) can be evaluated.

The in-house built out-of-plane shearography system with build-in FLIR A655 infrared (IR) camera is shown in Fig. 2. The choice of focusing on the out-of-plane surface displacement derivative was made as the out-of-plane deformation of delaminations and flat-bottom holes are expected to be predominant. The instrument details and its application for material characterization were previously reported in [34,37]. A Torus 532 CW laser (Laser Quantum, wavelength of 532 nm, operating at 200 mW optical power) was used to illuminate the surface of a specimen. The field of view (FOV) of the camera is about 300 × 300 mm^2 for a specimen at a distance of 1 m from the shearography instrument. Three halogen lamps operating at 500 W of electrical power were each used to apply a thermal loading to the specimen. For the GH mode, two symmetrically placed lamps [lamps 1 and 2, Fig. 2(a)] were at a distance of about 1 m from the test piece to heat it globally. The distance between the two lamps was about 0.8 m. For the SMH mode, only the third lamp [lamp 3, Fig. 2(b)] with a Fresnel lens (#32-685 by Edmund optics) was used to modulate the distribution of the heating profile on the object surface. The dimensions of the Fresnel lens are 170 × 170 mm^2 and its effective focal length is 254 mm. The distance between lamp 3 and the specimen was about 0.6 m. It can be noted that by adjusting the angles of the lamps and the position of the Fresnel lens, the uniformity of heat distribution was controlled, and then monitored by the IR camera. In this study, due to the illumination setup with the Fresnel lens and heating at an angle, the shape of the SMH was elliptical [Fig. 4 (d)]. The measured transient temperature with the IR camera during the inspection was further used for estimating the heat flux distribution on the specimen surface as an input for simulating thermal loading in Abaqus, which will be discussed later in Section 3.2.

The shearing device [Fig. 2(c)] was based on a Michelson interferometer with temporal phase-shifting achieved by a piezo-electric actuator PSH 4z from Piezosystem Jena. The five-step phase-shifting algorithm was selected due to its resulting accuracy [20]. Phase maps were sin/cos filtered with iterative circular averaging and median filters with a radius of 6 pixels and an aperture of 5 × 5 pixels respectively, further unwrapped with the branch-cut method [38]. The shear distance

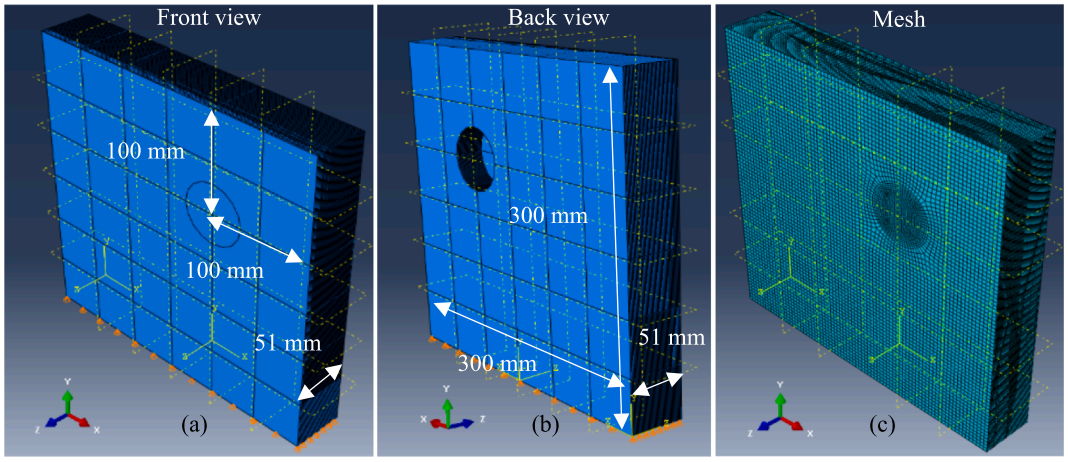

Fig. 3. Overview of the established 3D FEM model in Abaqus: (a) front view, (b) back view, (c) mesh.

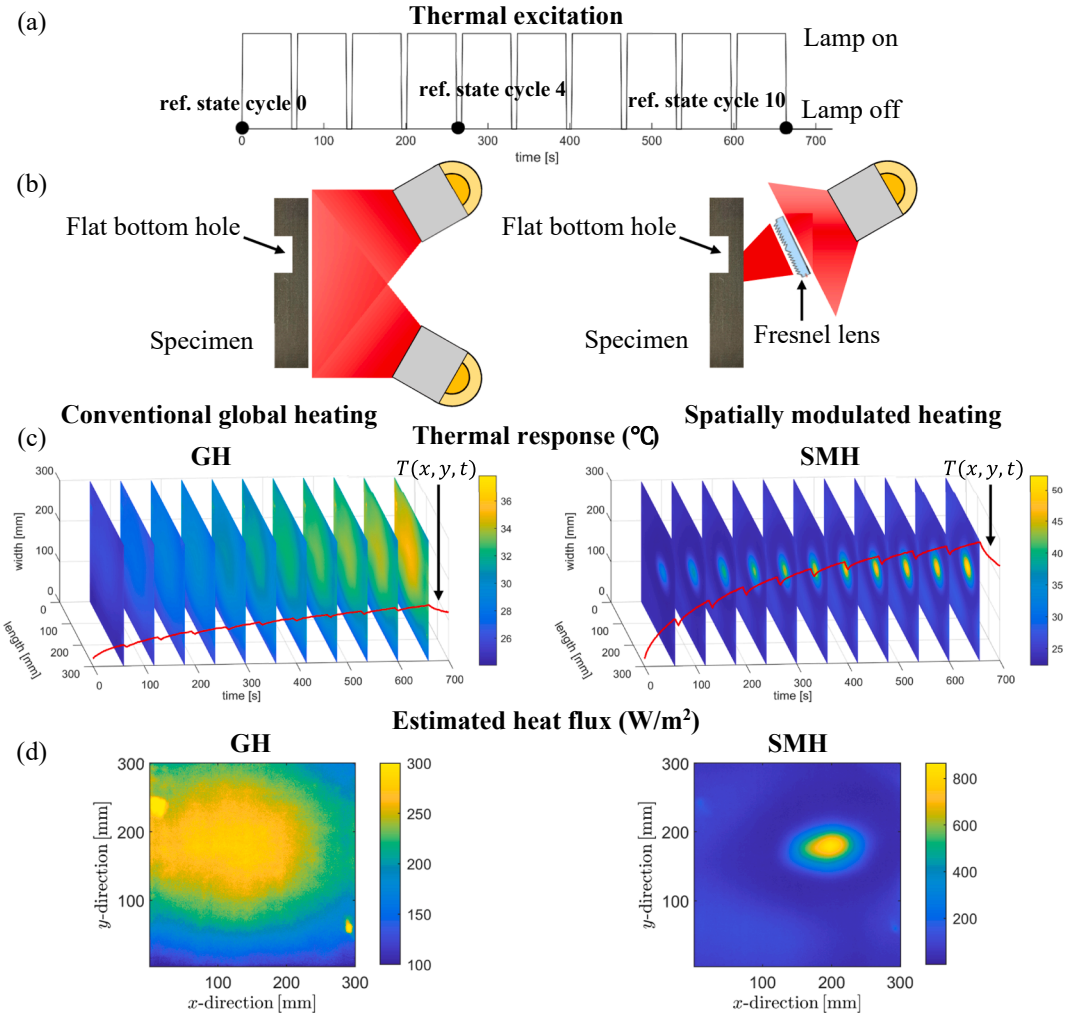

Fig. 4. Diagram of conventional global heating and spatially modulated heating as the Abaqus inputs of thermal loading: (a) thermal excitation, (b) diagram of conventional global heating and spatially modulated heating, (c) thermal response measured with the IR camera, (d) experimentally-determined heat flux for global heating and spatially modulated heating.

(δx) was calibrated over the FOV according to [37,39] and was found to be 7.8 ± 0.5 mm (mean ± std).

3. FEM model

FEM has been used to model both global heating and spatially modulated heating as the inputs of thermal loading with Abaqus. Considering that the layup of the test composite laminate ($[0/+45/90/-45]_{60}$) has repeating substructures, equivalent properties including effective laminate moduli [40–42] and effective laminate conductivities [43] can be determined for thick composite modelling to save computational time. The calculated equivalent thermal and mechanical properties of the test GFRP laminate for modelling can be found in [34]. In this section, the thick composite laminate model and the characterization of heat flux distributions of global heating and spatially modulated heating from measured transient temperature are reported.

3.1. Thick composite laminate model in Abaqus

The FEM model (in Fig. 3) was established in Abaqus CAE software. The front and the back views of the 3D model geometry are shown in Fig. 3 (a) and 3(b), respectively. It is important to note that an ideal mechanical boundary condition such as fully clamped is rather difficult to achieve in experiments as the thickness of the specimen is significant (~50 mm). Therefore the test panel was freestanding on the optical table during the shearography test, and to simulate this actual mechanical boundary condition, the displacement along the *y*-axis on the bottom surface is fixed [Fig. 3(a)]. To simulate thermal boundary conditions between the thick composite and environment, we chose a small value of heat transfer coefficient (2 $W \bullet m^{-2} \cdot K^{-1}$) for the model as the airflow in the lab is relatively small. The mesh of the model is shown in Fig. 3(c). There are 60 elements in the through-thickness direction (one element per equivalent layer). In the area with the defect, the mesh size is around 2×2 mm^2, while in the healthy region, the mesh size is around 4×4 mm^2 to make the computational time with high-performance computing (HPC) cluster reasonable. The C3D8RT element [44,45] was selected for the FEM model because of its advantages of saving computational time and its capabilities in coupled temperature-displacement analysis. The outputs include temperature and displacement. To validate the model, the simulated temperature will be compared with the transient temperature measured with the IR camera as well as thermocouples at representative locations. It can be mentioned that the out-of-plane displacement cannot be compared with shearography results (phase maps) directly, therefore a Matlab code has been developed to calculate simulated phase maps from the FEM displacement data. This can be realized by calculating the out-of-plane displacement derivative from the out-of-plane displacement (gap length: 2 mm) and then transferring the obtained displacement derivative data into Eq. (2). The

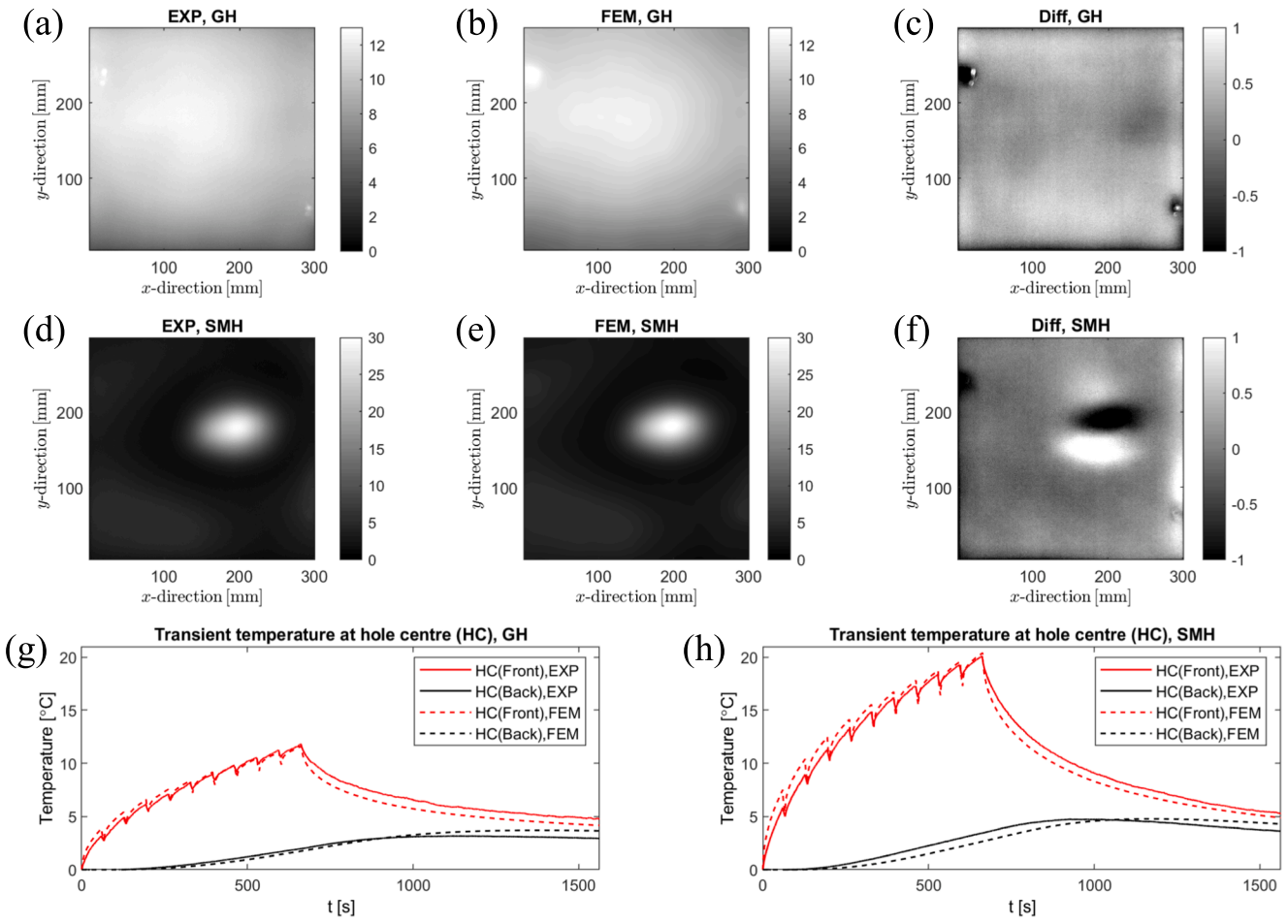

Fig. 5. Comparison of transient temperature between experiments (EXP) and simulations (FEM): (a)-(c): transient temperature for GH right after the 10th cycle of heating, measured by experiments, predicted by FEM, and the corresponding difference. (d)-(f) transient temperature for SMH right after the 10th cycle of heating, measured by experiments, predicted by FEM, and the corresponding difference. (g)-(h) transient temperature at the front and the back of the hole center with time for GH and SMH, respectively (Front measured with the IR, back measured with TCs). [Temperature unit in °C]

experimentally-determined calibrated shear distance over the specimen surface (Section 2.2) was implemented to obtain more accurate simulated phase maps. In this paper, the phase is chosen as a unit for comparison because it is the primary output from the shearography experiments.

3.2. *Characterization of heat flux distributions of global heating and spatially modulated heating*

The specifics of the thermal loading are given here. The test panel was heated from the front (defect-free side) by the halogen lamp(s). The heating scenario [Fig. 4(a)] is chosen as 10 cycles of 60 s heating and 7 s cooling, followed by a cooling phase (900 s), as preliminary analysis showed this gave a thermal penetration depth of about 25 mm (defect depth). The heating cycle was determined experimentally to get resolvable phase maps taken between the cycles. The transient temperature at the back of the hole center was measured with a thermocouple (TC) and the temperature rise was found to be several degrees Celsius. The related results will be reported later in Section 4.1.

Cyclic heating is selected in this paper over continuous heating to prevent overheating of the lamps. These gaps in the heating also allow intermediate speckle interferograms to be captured without overexposing the camera with the light of the lamps. These intermediate measurements will be used later to evaluate various reference states [Fig. 4(a)] on defect detection in Section 4.2. Conventional global heating and spatially modulated heating [Fig. 4(b)] were simulated in Abaqus as well as were applied to the specimen in experiments for analysis and comparison. The transient temperature on the specimen surface was measured with the IR camera for characterizing full-field heat flux distribution as the input of thermal loading in Abaqus.

We assume, that the heat flux of each heating cycle is the same as the positions and angles of the lamps are fixed. So the transient temperature of the first heating cycle [Fig. 4(c)] was used for estimating the heat flux distribution on the specimen surface. For heat conduction in a thick composite laminate, the transient temperature $T_1(x,y,t)$(for a short period) at each pixel (x, y) in the IR camera can be represented by the analytical solution of the semi-infinite solid with surface heat flux [46]:

$$T_1(x,y,t) = T_i + 2q(x,y)\left(\frac{t}{\pi\rho c_p k_z}\right)^{\frac{1}{2}} \tag{3}$$

where T_i is the initial temperature of the plate (20 °C, representing room temperature in the lab), $q(x,y)$ is the heat flux at pixel (x, y) on the front surface by the halogen lamp(s), and t is the heating time of the first cycle. Considering that the transient temperature in time can be measured with the IR camera, and the material properties including density ρ, the specific heat c_p, and the thermal conductivity in the through-thickness direction k_z are all known [34], the only unknown parameter is heat flux $q(x,y)$, which can therefore be estimated by a curve-fitting process [34]. With a loop to characterize heat flux pixel-by-pixel, the heat flux distribution over the specimen can be obtained. The estimated heat flux distributions by global heating and by spatially modulated heating are

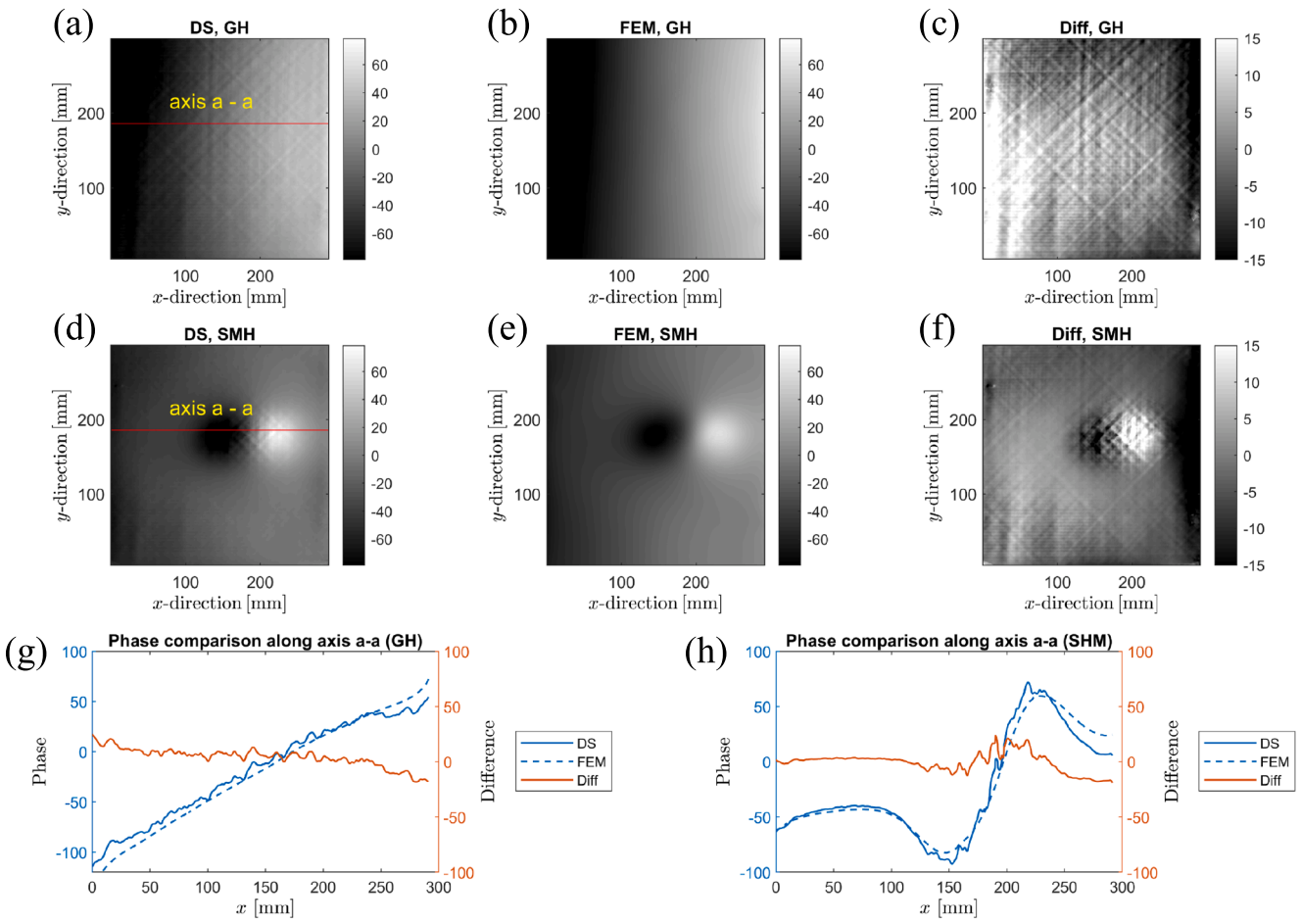

Fig. 6. Comparison of total phase maps between experiments (DS) and simulations (FEM): (a)-(c) total phase maps measured with DS, simulated by FEM, and the corresponding difference for GH, respectively. (d)-(f) total phase maps measured with DS, simulated by FEM, and the corresponding difference for SMH, respectively. (g)-(h) the comparison of phase along axis a-a for GH and SMH, respectively. [Phase unit in rad]

shown in Fig. 4(d). It can be seen that global heating was characterized as uniform heating with the variation of heat flux from 285 W/m^2 at the center to around 123 W/m^2 at the corner. The calculated uniformity of global heating is about 60%. Besides, as shown in Fig. 4(d), the heat is more concentrated for spatially modulated heating than for global heating. The maximum heat flux from spatially modulated heating is 3 to 4 times as large as that from global heating, while the average heat flux is about 40% of that from global heating. Because of this, it is expected that higher local deformations can be detected with spatially modulated heating. When the heating location of the region where energy is concentrated is close to the defect edge, it is expected that a strong defect signal will be obtained, which can therefore improve defect detection.

It should be addressed that Eq. (3) is a simplified solution without considering 3D heat transfer within the thick composite and heat transfer between the composite and environment, resulting in undervalued heat flux. In order to overcome this issue, a magnitude factor was introduced to modify the calculated heat flux distribution and this was estimated to be about 1.35 for this study.

4. Results and discussions

In this section, experimental and numerical results for shearography NDT of the deep defect are presented. First, a comparison between the experimental results and the numerical ones of the test GFRP panel (Fig. 1 and Fig. 3) for transient temperature and phase maps are reported in Section 4.1. Then the defect-induced responses subjected to GH and SMH are presented in Section 4.2. The impact of the reference status on shearography NDT of thick composites is discussed in Section 4.3. In experiments, it can be noted that the sets of phase-shifted speckle interferograms were recorded continuously with the shearography instrument. All these sets were processed and built up, generating the phase map that reveals the development of the out-of-plane displacement gradient over the inspection time. The unit of phase is radian, and in this instrument-specimen geometry (Fig. 2), 1 rad corresponds to about 5.4 $\mu\varepsilon$.

4.1. Comparison in temperature and phase between experiments and simulations

This section describes the model validation for temperature changes using experimental results. Fig. 5(a) and 5(b) are 2D plots of transient temperature for GH (right after the 10th cycle of heating) measured with the IR camera and predicted by FEM, respectively. The corresponding difference is shown in Fig. 5(c). Fig. 5(d)-5(f) are 2D plots of transient temperature for SMH measured with the IR camera, predicted by FEM, and the corresponding difference, respectively, the time instant is right after the 10th cycle of heating as well. It can be noted that the initial temperature of the specimen before heating is around 20.0 °C, which was subtracted from the data in the figure. The maximum temperature increase by SMH (~30 °C) is about 2.5 times as large as that by GH (~12 °C). The difference between experiments and simulations is ±1.0 °C for GH and ±1.5 °C for SMH, respectively. This comparison shows a good agreement in transient temperature between the

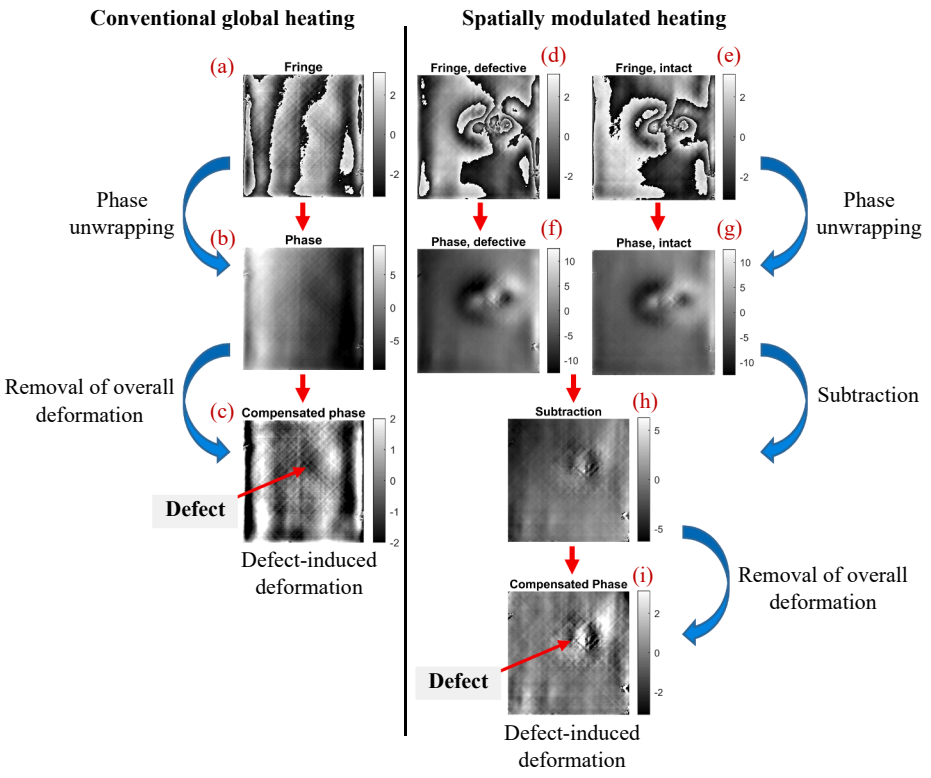

Fig. 7. Data processing for obtaining defect-induced phase maps from original phase maps [Phase unit in rad]

experimental results and the FEM ones. For GH the temperature is uniform with variation (10.2 ± 1.9 °C), while for SMH the temperature is more focused due to the more concentrated heat flux. Fig. 5(g) and 5(h) show the transient temperature at the front and the back of the hole center with time for GH and SMH, respectively. The solid lines indicate transient temperature from experiments, and the dotted lines indicate those from simulations.

The model comparison of simulated phase maps with measured phase maps is given here. The initial status before heating and the final status right after the 10th cycle of heating were applied to build up total phase maps for comparison as they are representative states during the inspection. Fig. 6(a) and 6(b) are total phase maps (for GH) measured with shearography and simulated by FEM, respectively. The maximum phase values from the experiment and simulation are both close to 60 rad, which indicates a good agreement between the experimental results and the FEM ones for GH. The corresponding difference is shown in Fig. 6(c). The difference between experiment and simulation is around 6 rad at the center and ±16 rad near the edge for the total phase range −100 to +60 rad. Fig. 6(d) and 6(e) are total phase maps (for SMH) measured with shearography and predicted by FEM, respectively. The maximum phase values by experiment and by simulation for SMH are also close to each other (~60 rad). The corresponding difference is shown in Fig. 6(f), where the difference between experiment and simulation is around −10 to +20 rad near the modulated heating area and −16 to −10 rad near the right edge for the total phase range −80 to +60 rad. For both GH and SMH, it is shown that the difference between experiments and simulations near the edge area is a bit large. This may be because it is close to the edge of the FOV where the shear calibration is less reliable. Besides, the factors such as non-ideal boundary conditions in the experimental set-up and lower signal-to-noise ratio at the corners due to the non-uniform distribution of the illuminating laser light may also contribute to this error. Shearography measurement uncertainty right at the boundary at the scale of shear distance (~7.8 mm) might contribute, which is expected to be small with reference to specimen size (~300 mm). For the analysis, we only took the effective area of inspection excluding shear uncertainty.

Fig. 6(g) and 6(h) show the phase comparison along axis a-a for GH and SMH, respectively. The blue lines in Fig. 6(g) and 6(h) represent the phases by shearography (solid lines) and by FEM (dotted lines), respectively. The corresponding difference is shown by an orange line. It is shown that the phase curves obtained by experiments have a variation of about 3 rad standard deviation [Fig. 6(g)]. This variation, which appears as lines with angles of 0°, ±45°, 90° in Fig. 6(c), is assumed to rise from the fiber deformation (e.g. related to fiber layup) which can be considered here as background noise. While in FEM, we homogenised the fiber and resin per equivalent layer, therefore the phase curves by simulation are smooth.

4.2. Analysis of defect-induced phase

This section reports on the analysis of defect-induced phase for GH and SMH, respectively. The process for obtaining defect-induced phase from original phase maps is shown in Fig. 7. Take conventional global heating as an example for the explanation. First the phase fringe maps [Fig. 7 (a), wrapped phases] were obtained by comparison of two deformation states of the specimen. After phase unwrapping, the phase maps are related to surface deformation. The original phase maps [$\delta\phi_{total}$, Fig. 7(b)] contain information about both defect-induced deformation $\delta\phi_{DIP}$ and overall deformation $\delta\phi_{OD}$ (background signal). In order to extract defect-induced deformation ($\delta\phi_{DIP}$), a phase compensation process was performed. First a fitting surface was created by using polynomial fitting to represent overall deformation, and the subtraction between the original phase map and the fitting surface gives $\delta\phi_{DIP}$ [Fig. 7(c)], which represents defect–induced phase (defect signal):

$$\delta\phi_{DIP} = \delta\phi_{total} - \delta\phi_{OD} \tag{4}$$

For the SMH scenario, the fitting plane created by the polynomial fitting of the original phase is no longer useful due to the spatial modulation in heat flux. In order to overcome this problem, we repeated the shearography experiments (the same heating scenario, the same

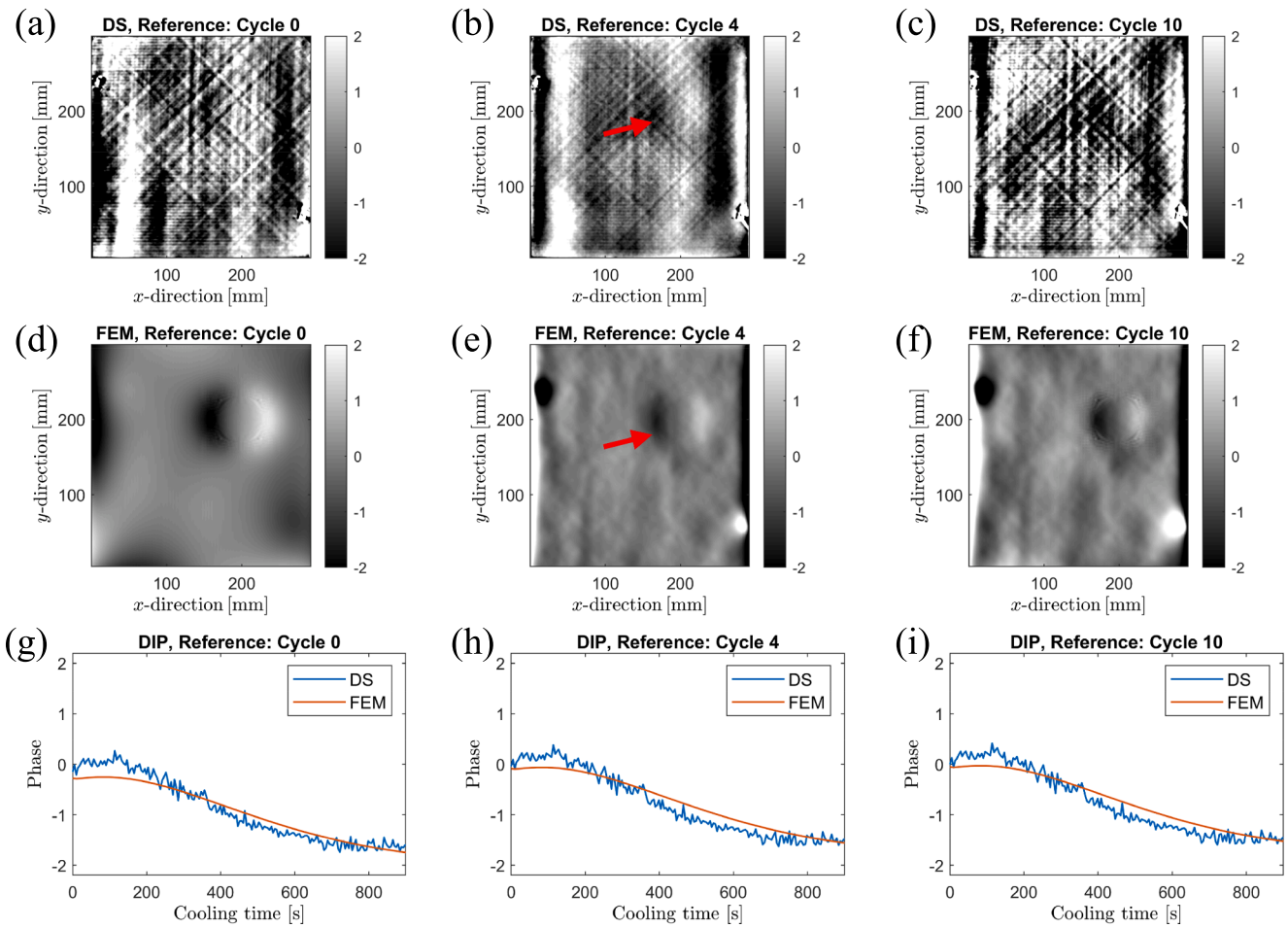

Fig. 8. Defect-induced phase (DIP) maps by GH: (a)-(c) defect-induced phase maps by shearography (DS) for the three reference status, respectively. (d)-(f) defect-induced phase maps by FEM for the three reference status, respectively. (g)-(i) the defect-induced phase changes with cooling time for the three reference status, respectively. [Phase unit in rad]

boundary condition) by replacing the defective plate (D60-Z25) with an intact plate (defect-free). The subtraction gives $\delta\phi_{sub}$ [Fig. 7(h)],

$$\delta\phi_{sub} = \delta\phi_{defect} - \delta\phi_{intact} \tag{5}$$

where $\delta\phi_{defect}$ represents the phase from the defective plate, and $\delta\phi_{intact}$ represents the phase from the intact plate. Their subtraction ($\delta\phi_{sub}$) can help to remove overall deformation. Then a similar phase compensation process (similar to GH scenario, creating a fitting surface from $\delta\phi_{sub}$, and then subtracting it) by using polynomial fitting was performed to further remove overall deformation and therefore the defect-induced phase [$\delta\phi_{DIP}$, Fig. 7(i)] for SMH was obtained.

The above data processing method was performed for experimental data as well as FEM data. We should acknowledge a limitation of the method is needing a reference undamaged panel for extracting defect-induced deformation by SMH, during which extra errors can also be introduced. The issue of extracting defect deformation by other methods will be the objective of future work. To reduce the extra errors in this method as much as possible, the test panel and the reference undamaged panel under investigation were cut with the same dimensions from the same larger GFRP plate. Besides, the white painting on the surfaces of the panels [Fig. 1(a)] was sprayed in the same manner. It can be noted that after the phase compensation process, the obtained defect-induced phase from FEM data can be seen as a purely defect signal, while that from experimental data may still contain noise resulting from fiber-related deformation and speckle-related errors. These types of noise were not considered in modelling due to their complexity.

The influence of reference states [Fig. 4(a)] on deep defect detection with shearography was investigated by analysis of defect-induced phase. Fig. 8 shows defect-induced phase maps corresponding to three representative reference states by GH, where the final states were at the same time instant during cooling. The three reference states include the 0th cycle of heating (representing status before loading), the 4th cycle of heating (representing status after 240 s of loading), and the 10th cycle of heating (representing status right after loading). Fig. 8(a)–8(c) are defect-induced phase maps measured with shearography for the three reference states, and Fig. 8(d)-8(f) are the ones predicted by FEM. It is shown that as the reference status differs, the defect-induced phase map may change and therefore the efficacy of defect detection may vary. The defect (D60-Z25) is detectable from all the three simulated phase maps by FEM [Fig. 8(d)–8(f)]. However in experiments, it is detectable only from the reference status at the 4th cycle of heating [Fig. 8(b)], which has a relatively good agreement with Fig. 8(e) from FEM. While for the other two reference states, the defect is barely detected [Fig. 8(a)] or partially detected [Fig. 8(c)] possibly due to the influence of the fiber-related deformation. Fig. 8(g)-8(i) show the defect-induced phase changes with cooling time for the three different reference states. An average defect-induced phase value of a 3 × 3 pixels region near the edge of the artificial defect was selected where the maximum defect signal was expected to occur. It should be noted that this selected region should also avoid the influence of fiber deformation as much as possible. The blue lines are from experimental data and the orange ones are from FEM data. It is shown that despite the influence of fiber deformation, the comparison of the maximum defect signal between shearography and

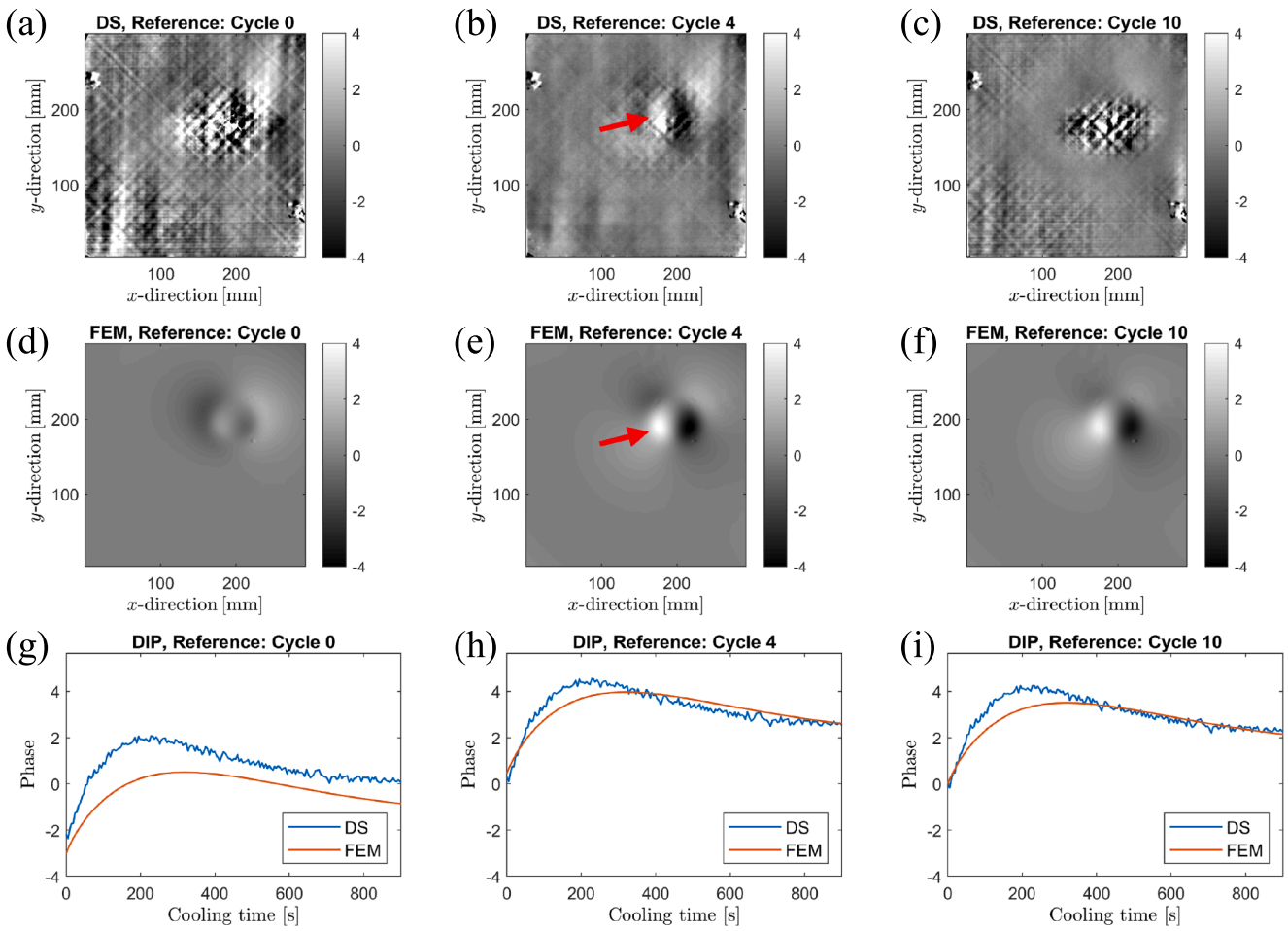

Fig. 9. Defect-induced phase (DIP) map by SMH: (a)-(c) defect-induced phase maps by shearography (DS) for the three reference status, respectively. (d)-(f) defect-induced phase maps by FEM for the three reference status, respectively. (g)-(i) the defect-induced phase changes with cooling time for the three reference status, respectively. [Phase unit in rad]

FEM still shows a good agreement. Although the defect can be detected from the modelling point of view, nevertheless, in real experiments, the actual detection results may vary a lot due to choosing different reference sets of images. From the point of reducing the noise from fiber-related deformation, choosing the reference status during heating is favorable in comparison with the other two reference states, This is further explained in Section 4.3.

The defect-induced phase maps by SMH are given in Fig. 9. The final states were at the same cooling time instant, and similar to Fig. 8, the same three different reference states (0th, 4th, 10th cycles of heating) were selected for comparison. Fig. 9(a)-9(c) are defect-induced phase maps obtained by shearography data for the three different reference states, and Fig. 9(d)-9(f) are the ones obtained by FEM data. It is also shown that as the reference status is different, the efficacy of defect detection may vary from the experimental results by shearography. This phenomenon is similar to the GH scenario, and a possible explanation can be found in Section 4.3. The comparison between shearography and FEM has a good agreement when selecting reference status as the 4th cycle of heating [Fig. 9(b) and Fig. 9(e)]. While for the other two reference status cases, the similarity between shearography and FEM is not ideal. This will also be discussed in Section 4.3 as well. Fig. 9(g)-9(i) show the defect-induced phase changes with cooling time, where an average defect-induced phase value of a 3 × 3 pixels region near the defect edge was selected to indicate the defect signal. The blue lines are from experimental data and the orange ones are from FEM data. There is a larger difference in defect signal by SMH [Fig. 9(g)] than that by GH. This is because for the SMH studied in this paper, the heat flux is more concentrated than for GH, and the maximum heat flux by SMH is higher (around 3 to 4 times as that by GH), therefore the fiber deformation by SMH has a greater impact on the defect-induced phase maps compared with that by GH. It can be seen in Fig. 9(g)–9(i), that the defect-induced phase curves by experiments and by simulations still show a good similarity.

Table 1
Summary of maximum defect signal by SMH and GH, respectively.

		SMH	GH
Average heat flux (W/m^2)		~90	~220
Maximum defect signal in phase (rad)	DS	~4.5	~1.5
	FEM	~4.0	~1.5

The experimental and numerical results for GH (Fig. 8) and SMH (Fig. 9) are summarized in Table 1. The maximum defect signal value is obtained from the results of reference status at the 4th cycle of heating since it shows a better performance in defect detection than the results from the other two reference status cases.

As shown in this table, the average heat flux by SMH is only about 40% of that by GH, but the maximum defect signal by SMH is around 2 to 3 times as large as that by GH, which is a significant improvement in defect detection. The defect-induced phase maps by SMH [Fig. 9(b) and 9(e)] also show a better performance in defect detection than those by GH [Fig. 8(b) and 8(e)].

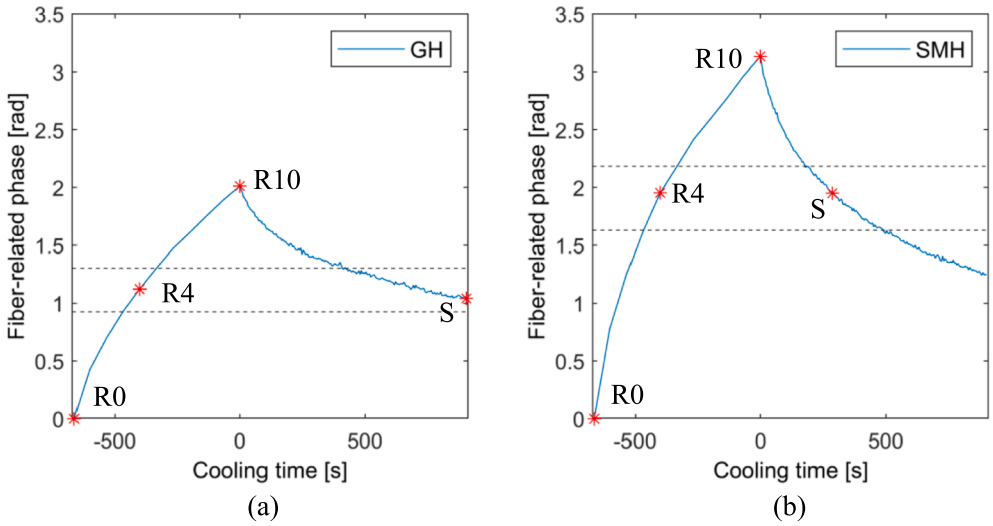

Fig. 10. The average fiber deformation with time during the inspection (a) by GH, (b) by SMH.

4.3. Discussions of reference status on deep defect detection

It has been shown that the efficacy of shearography NDT of the deep defect in thick composite varies when selecting a different reference status [e.g. Fig. 8(d)–8(f)]. This could be due to their difference in temperature at the three reference states, indicating that the defect responses at the three reference states can vary. Hence, although the final states are the same, the comparison between the two states can be different, resulting in a variation in defect detection efficacy.

For both GH and SMH, it was also shown that the defect-induced phase map by shearography has a good agreement with that by FEM when selecting the reference state as the 4th cycle of heating. Nevertheless, the similarity between shearography and FEM results is not good when selecting the other two reference states for comparison. This could be because for these two reference status cases from shearography, the influence of fiber deformation is significant in the defect-induced phase maps, while as mentioned before, the fiber deformation was not considered in the modelling. Below, we will discuss this in more detail.

The average fiber deformation over time during the inspection is shown in Fig. 10. The reference status is before loading. This figure was plotted by averaging the defect-induced phase maps of a selected region at each time instant. Since the defect-induced phase contains positive as well as negative values, their absolute values were averaged to represent the average fiber-related deformation during the inspection. The origin of time was right after the 10th cycle of heating, so the time with negative sign represents the cycling heating phase, and the time with positive sign represents the cooling phase.

It is shown that the maximum fiber-related optical phases are around 2.0 rad (GH) and 3.0 rad (SMH), respectively, which are comparable to the corresponding defect signal. In Fig. 10, point R4 represents the status of fiber deformation at the end of the 4th cycle of heating and point S represents the final status selected in Section 4.2. We can assume that the fiber-related optical phases have no apparent difference for these two deformation states, therefore when selecting reference status as right after the 4th cycle of heating (R4), it yields relatively good results in defect detection as the influence of fiber deformation is reduced significantly. While selecting another reference status such as the 0th cycle of heating (R0) or the 10th cycle of heating (R10), the fiber-related phase will still have a great impact on the defect-induced phase maps, therefore it may affect significantly the efficacy of shearography inspection. A suggested rule for selecting the suitable reference and final states for shearography NDT of thick composites will be, to try to reduce the fiber-related phase as much as possible while keeping the defect signal as high as possible. For this sample, this can be done by a reference status of 40% of the overall heating time.

5. Conclusions

In this work, FEM-assisted shearography with spatially modulated heating has been proposed and applied for improving the detection of deep defects in thick composite laminates. Both conventional global heating and spatially modulated heating were performed experimentally and modelled numerically for shearography NDT. The heat flux distribution on the specimen surface was taken into consideration in this study, which is rarely reported in defect detection with shearography. The influence of different reference states on shearography NDT of thick composites was studied in this paper. Current results showed that SMH has one or a combination of the following advantages: energy concentration, high defect signal, deeper defect detection, improved edge detection of a defect, and potentially fast inspection. The conclusions obtained from the present study are as follow:

(1) With spatially modulated heating it is possible to improve the detection of the deeply buried defect in the thick composite laminate. As shown in this paper, the maximum defect signal by SMH can be 2 to 3 times that from global heating with about 40% of the average heat flux (Table 1). This result is promising for improving deep defect detection even with low-power heating sources. Nevertheless, it should be addressed that due to non-uniform heating and the complex global deformation with SMH, additional measurements of a similar and defect-free reference sample are currently necessary to compare that of a defective plate. In order to use the presented method as a reference-free one, some advanced algorithms, e.g. phase compensation by combining analytical solutions of thermal deformation or prediction by FEM may be useful to overcome this problem.

(2) The efficacy of shearography NDT of the deeply buried defect in the thick composite laminate can vary when selecting different reference states, in which the issue of fiber-related deformation on deep defect detection should be treated carefully when applying thermal loading. A suggested rule for selecting the suitable reference states (as well as signal states) is, to reduce the background phase (e.g. fiber-related) as much as possible while keeping the defect signal high. In this paper it was achieved by selecting the reference status as 40% of the total heating time.

(3) The current FEM model has the drawback of not considering fiber-related deformation and speckle-related errors. However it is acceptable for the sake of saving computational time.

It can be noted that the efficacy of defect detection by the proposed SMH can vary greatly depending on the heating positions. The detection is expected to be more efficient as the heating position is close to the defect. Nevertheless, in a real inspection the location of a defect usually remains unknown beforehand. To cope with this problem, a combination of GH and SMH for shearography NDT can be a reasonable solution for the detection of deep defects, that is, first applying GH for overall searching of suspicious areas, and then applying SMH for detailed characterization of deep defects.

In this study, we used an elliptical shape pattern with the proposed SMH method, as a rational result of the illumination setup with the Fresnel lens and heating at an angle. Other shapes or other types of SMH, e.g. by using multiple Fresnel lenses, can be investigated in the future. Besides, developing some advanced algorithms to extract defect-induced deformation can be a promising subject for future work. For example, phase compensation by combining analytical solutions of thermal deformation or prediction by FEM.

CRediT authorship contribution statement

Nan Tao: Methodology, Formal analysis, Software, Investigation, Writing – original draft, Visualization. **Andrei G. Anisimov:** Conceptualization, Software, Supervision, Writing – review & editing, Visualization. **Roger M. Groves:** Supervision, Writing – review & editing, Project administration, Funding acquisition.

Declaration of Competing Interest

The authors declare that they have no known competing financial interests or personal relationships that could have appeared to influence the work reported in this paper.

Data availability

Data will be made available on request.

Acknowledgment

We would like to thank Damen Shipyards Group and namely Marcel Elenbaas for the materials and the industrial feedback. This research was supported by the Operationeel Programma Zuid-Nederland (Op–Zuid) Project as part of the Dutch Composite Maintenance Centre (DCMC), supported by the Europees Fonds voor Regionale Ontwikkeling (EFRO) and the North Brabant province of the Netherlands.

Appendix A. Supplementary material

Supplementary data to this article can be found online at https://doi.org/10.1016/j.compstruct.2022.115980.

References

[1] Nsengiyumva W, Zhong S, Lin J, Zhang Q, Zhong J, Huang Y. Advances, limitations and prospects of nondestructive testing and evaluation of thick composites and sandwich structures: A state-of-the-art review. Compos Struct 2021;256:112951.
[2] Ibrahim ME. Nondestructive evaluation of thick-section composites and sandwich structures: a review. Compos A Appl Sci Manuf 2014;64:36–48.
[3] Greene E. Inspection techniques for marine composite construction and NDE. Report No SSC-463, United States Ship Structure Committee, Washington, DC 2012.
[4] Tran P, Ghazlan A, Nguyen TP, Gravina R. Experimental and theoretical damage assessment in advanced marine composites. In: Pemberton R, Summerscales J, Graham-Jones J, editors. Marine Composites, Woodhead Publishing; 2019, p. 55–84.
[5] Groves RM. Inspection and Monitoring of Composite Aircraft Structures. In: Beaumont PWR, Zweben CH, editors. Comprehensive Composite Materials II. Oxford: Elsevier; 2018. p. 300–11.
[6] Jerome P. Composite materials in the Airbus A380-from history to future. Beijing: Proceedings 13th International Conference on Composite Materials (ICCM-13); 2001.
[7] Zhang P. Offshore wind turbines. In: Pemberton R, Summerscales J, Graham-Jones J, editors. Marine Composites, Woodhead Publishing; 2019, p. 317–44.
[8] Hou Y, Li L, Koo JH. Thick-Section Epoxy Composites. In: Chowdhury MA, Armenta JLR, Rahman MM, Asiri A, Inamuddin, editors. Composite Materials, Rijeka: IntechOpen; 2021.
[9] Alleman G. The effects of different cure cycles on the mechanical performance of thick-walled composites 2018.
[10] Maierhofer C, Krankenhagen R, Röllig M. Application of thermographic testing for the characterization of impact damage during and after impact load. Compos B Eng 2019;173:106899.
[11] Montanini R, Freni F. Non-destructive evaluation of thick glass fiber-reinforced composites by means of optically excited lock-in thermography. Compos A Appl Sci Manuf 2012;43(11):2075–82.
[12] Revel GM, Pandarese G, Cavuto A. Advanced ultrasonic non-destructive testing for damage detection on thick and curved composite elements for constructions. J Sandwich Struct Mater 2013;15(1):5–24.
[13] Lambrineas P, Davis JR, Suendermann B, Wells P, Thomson KR, Woodward RL, et al. X-ray computed tomography examination of inshore minehunter hull composite material. NDT and E Int 1991;24(4):207–13.
[14] Tan KT, Watanabe N, Iwahori Y. X-ray radiography and micro-computed tomography examination of damage characteristics in stitched composites subjected to impact loading. Compos B Eng 2011;42(4):874–84.
[15] Mehdikhani M, Straumit I, Gorbatikh L, Lomov SV. Detailed characterization of voids in multidirectional carbon fiber/epoxy composite laminates using X-ray micro-computed tomography. Compos A Appl Sci Manuf 2019;125:105532.
[16] Sinha L, Das D, Nayak AN, Sahu SK. Experimental and numerical study on free vibration characteristics of laminated composite plate with/without cut-out. Compos Struct 2021;256:113051.
[17] Sahu SK, Das P. Experimental and numerical studies on vibration of laminated composite beam with transverse multiple cracks. Mech Syst Sig Process 2020;135:106398.
[18] Hung YY, Chen YS, Ng SP, Liu L, Huang YH, Luk BL, et al. Review and comparison of shearography and active thermography for nondestructive evaluation. Mater Sci Eng: R: Rep 2009;64(5-6):73–112.
[19] Yang R, He Y. Optically and non-optically excited thermography for composites: a review. Infrared Phys Technol 2016;75:26–50.
[20] Francis D, Tatam RP, Groves RM. Shearography technology and applications: a review. Meas Sci Technol 2010;21(10):102001.
[21] Hung YY. Shearography for non-destructive evaluation of composite structures. Opt Lasers Eng 1996;24(2-3):161–82.
[22] Zhao Q, Dan X, Sun F, Wang Y, Wu S, Yang L. Digital Shearography for NDT : Phase Measurement Technique and Recent Developments. Applied Sciences (Switzerland) 2018;8.
[23] De Angelis G, Meo M, Almond DP, Pickering SG, Angioni SL. A new technique to detect defect size and depth in composite structures using digital shearography and unconstrained optimization. NDT and E Int 2012;45(1):91–6.
[24] Liu Z, Gao J, Xie H, Wallace P. NDT capability of digital shearography for different materials. Opt Lasers Eng 2011;49(12):1462–9.
[25] Akbari D, Soltani N, Farahani M. Numerical and experimental investigation of defect detection in polymer materials by means of digital shearography with thermal loading. Proc Instit Mech Eng Part B: J Eng Manuf 2013;227(3):430–42.
[26] Garnier C, Pastor M-L, Eyma F, Lorrain B. The detection of aeronautical defects in situ on composite structures using Non Destructive Testing. Compos Struct 2011;93(5):1328–36.
[27] Newman JW. 7.13 Shearography Nondestructive Testing of Composites. In: Beaumont PWR, Zweben CH, editors. Comprehensive Composite Materials II. Oxford: Elsevier; 2018. p. 270–90.
[28] Krutul EC, Groves RM. Opto-mechanical modelling and experimental approach to the measurement of aerospace materials using shearography and thermal loading. In: Bodermann B, editor. Modeling Aspects in Optical Metrology III, vol. 8083. SPIE; 2011. p. 434–42.
[29] Jiang H, Ma Y, Dai M, Dai X, Yang F, He X. Panoramic dual-directional shearography assisted by a bi-mirror. Appl Opt 2020;59:5812–20.
[30] Bison PG, Bressan C, Cavaccini G, Ciliberto A, Grinzato EG. NDE of composite materials by thermal method and shearography. In: Wurzbach RN, Burleigh DD, editors. Thermosense XIX: An International Conference on Thermal Sensing and Imaging Diagnostic Applications, vol. 3056. SPIE; 1997. p. 220–9.
[31] Buchta D, Heinemann C, Pedrini G, Krekel C, Osten W. Combination of FEM simulations and shearography for defect detection on artwork. Strain 2018;54(3):e12269.
[32] Vandenrijt J-F, Xiong H, Lequesne C, Blain P, Georges M. Shearography inspection of monolithic CFRP composites: finite element modeling approach for assessing an adequate strategy of artificial defects representing delamination. In: Lehmann P, Osten W, Jr. AAG, editors. Optical Measurement Systems for Industrial Inspection XI, vol. 11056, SPIE; 2019, p. 107–13.
[33] di Scalea FL, Spicer JB, Green RE. Electronic Shearography with Thermal Loading for Detecting Debonds in Thick Polyurethane/ Steel Panels for Marine Applications. Res Nondestr Eval 2000;12(1):43–51.

[34] Tao N, Anisimov AG, Groves RM. Shearography non-destructive testing of thick GFRP laminates: Numerical and experimental study on defect detection with thermal loading. Compos Struct 2022;282:115008.
[35] Tao N, Anisimov AG, Groves RM. Spatially modulated thermal excitations for shearography non-destructive inspection of thick composites. In: Lehmann P, Osten W, Jr. AAG, editors. Optical Measurement Systems for Industrial Inspection XII, vol. 11782, SPIE; 2021, p. 183–8.
[36] Steinchen W, Yang L. Digital shearography: theory and application of digital speckle pattern shearing interferometry. vol. 100. CCH; 2003.
[37] Anisimov AG, Serikova MG, Groves RM. 3D shape shearography technique for surface strain measurement of free-form objects. Appl Opt 2019;58:498–508.
[38] Ghiglia DC, Pritt MD. Two-dimensional phase unwrapping: theory, algorithms, and software. New York: Wiley; 1998.
[39] Goto DT, Groves RM. Error analysis of 3D shearography using finite-element modelling. In: Gorecki C, Asundi AK, Osten W, editors. Optical Micro- and Nanometrology III, vol. 7718. SPIE; 2010. p. 281–92.
[40] van Hoorn N, Kassapoglou C, van den Brink WM. Impact response prediction and sensitivity analysis of thick laminated composite plates. Techreport NLR-TP-2019-529 2020.
[41] Sun CT, Li S. Three-Dimensional Effective Elastic Constants for Thick Laminates. J Compos Mater 1988;22:629–39.
[42] Chan WS, Lin CY, Liang YC, Hwu C. Equivalent thermal expansion coefficients of lumped layer in laminated composites. Compos Sci Technol 2006;66(14):2402–8.
[43] Kulkarni MR, Brady RP. A model of global thermal conductivity in laminated carbon/carbon composites. Compos Sci Technol 1997;57(3):277–85.
[44] Li Y, Zhang W, Yang Z, Zhang J, Tao S. Low-velocity impact damage characterization of carbon fiber reinforced polymer (CFRP) using infrared thermography. Infrared Phys Technol 2016;76:91–102.
[45] Cheng H, Gao J, Kafka OL, Zhang K, Luo B, Liu WK. A micro-scale cutting model for UD CFRP composites with thermo-mechanical coupling. Compos Sci Technol 2017;153:18–31.
[46] Bergman TL, Lavine AS, Incropera FP, DeWitt DP. Fundamentals of heat and mass transfer. Wiley; 2017.